geotechnics

Article

Influence of Temperature Effects on CPT in Granular Soils by Discrete Element Modeling in 3D

Yun Huang [1], Weichen Sun [2], Hongyi You [3] and Kai Wu [3,*]

1 PowerChina Chendu Engineering Corporation Limited, Chendu 610000, China; huangyun@chidi.com.cn
2 Sohool of Civil Engineering, Chongqing University, Chongqing 400045, China; wcsun@cqu.edu.cn
3 School of Transportation, Southeast University, Nanjing 210096, China; hongyiyou03@163.com
* Correspondence: wukai2018@seu.edu.cn

Abstract: This study employs a 3D discrete element method (DEM) to simulate cone penetration tests (CPTs) in granular soils, taking into account the effect of temperature. A coupled thermal mechanical model is developed to allow for heat transfer and storage in the granular materials. The CPT simulations are conducted on granular samples prepared at various temperatures, with the specific heat and velocity of thermal conductivity being identified as two critical factors that influence sample heating time. Additionally, the thermal expansion coefficient is a crucial parameter that is closely related to the porosity of the sample. As the sample temperature increases, the particles expand, resulting in an increase in cone resistance.

Keywords: DEM; CPT; temperature; cone resistance; specific heat

check for updates

Citation: Huang, Y.; Sun, W.; You, H.; Wu, K. Influence of Temperature Effects on CPT in Granular Soils by Discrete Element Modeling in 3D. *Geotechnics* **2023**, *3*, 624–637. https://doi.org/10.3390/geotechnics3030034

Academic Editor: Abbas Taheri

Received: 9 May 2023
Revised: 19 June 2023
Accepted: 5 July 2023
Published: 7 July 2023

Copyright: © 2023 by the authors. Licensee MDPI, Basel, Switzerland. This article is an open access article distributed under the terms and conditions of the Creative Commons Attribution (CC BY) license (https://creativecommons.org/licenses/by/4.0/).

1. Introduction

The expansion and contraction of materials upon heating and cooling are ubiquitous phenomena that impact many aspects of our daily lives. Heating a material increases the range of motion of its molecules, causing it to expand, while cooling has the opposite effect by weakening the molecular kinetic energy. Such fundamental material properties have significant implications for civil engineering. For example, cracking during cold seasons and rutting during hot seasons can reduce the durability of asphalt pavements. In addition, the effects of temperature on the deformation of rocks and the mechanical behavior of granular soils are critical considerations for engineering safety. In regions where the ground temperature fluctuates considerably between day and night, soil properties such as density, pore pressure, and shear strength significantly vary [1,2]. Studies have found that, except for kaolinitic soil, most soils exhibit slightly increased plasticity and unconfined compressive strength as the temperature rises [3]. To address the unique challenges posed by temperature effects in civil engineering, some engineers have employed thermal reinforcement methods to reinforce special foundations. Therefore, extensive research is needed to fully understand the mechanical behavior of granular soils under temperature effects.

The cone penetration test (CPT) is widely used to estimate soil strength during site surveys [4,5]. This test involves inserting a cone-shaped penetrometer into the soil at a constant velocity to obtain a continuous vertical profile of cone tip resistance (q_c), sleeve friction (f_s), pore water pressure (u_2), and other factors at every inch of the subsoil depth [6]. CPT technology has proven invaluable in solving numerous engineering challenges [7,8]. However, the influence of temperature on soil behavior can complicate the interpretation of CPT results. For instance, Kim et al. [9] reported that temperature effects can produce unreliable cone tip resistance measurements. Due to the extensive resources and time demands of experimental research on the impact of temperature on CPTU testing results, numerical simulation has emerged as an alternative approach.

Numerical simulations are commonly used to investigate the effects of temperature on soils. For instance, Staniec et al. [10] developed a finite-element model that utilizes a transient heat conduction differential equation to simulate the temperature distribution within a given domain. They also incorporated an energy balance at the soil surface to enhance the accuracy of their model. Gao et al. [11] investigated the temperature dependence of soil hydraulic properties and found that temperature variations affect soil particles, porosity, and the interactive surface between liquid and solid phases, especially in heavy loams with high clay content. Since soil particles are discrete, the discrete element method (DEM) has emerged as a powerful tool for studying the macro- and micro-behavior of granular soils. DEM, first proposed by Cundall and Stack in 1979 [12], calculates the motions of each particle in a granular system using Newton's law. This method provides an insight into the relationship between the macroscopic behavior of a granular assembly and the microscopic motions of its particles. DEM has been used in several previous studies on cone penetration tests (CPT). For example, Jiang et al. [13–15] employed DEM simulations to investigate the mechanism of the inclined CPT in granular ground. They found that soils around the cone tip exhibit complex displacement paths at different positions along the inclined penetration, while friction only exerts significant effects on the soils adjacent to the penetrometer side and tip. Butlanska et al. [16–19] investigated the impact of radial walls on cone penetration testing (CPT) in a virtual calibration chamber (VCC) based on the discrete element method (DEM). Their results indicated that the asymptotic CPT values in the VCC agreed with those obtained from physical experiments. Ciantia et al. [20] investigated the effect of crushable grains on CPT tip resistance and found that crushing disrupted the buttressing effect of chamber walls on the cone. McDowell et al. [21] proposed a particle refinement method that reduced the particle size near the cone tip for a more accurate modeling of CPT in soils with decreasing particle numbers. Falagush et al. [22,23] compared DEM simulations of CPT with analytical solutions based on cavity expansion and found a close agreement between both methods. Zhong et al. [24] investigated the penetration characteristics of snake skin-inspired pile using DEM. Their research demonstrated that the snakeskin-inspired pile has a greater shaft resistance, and causes obvious soil disturbance with respect to soil displacement and particle rotation compared with the reference pile. Shi et al. [25] modelled the screw pile penetration in loose granular assemblies considering the effect of drilling velocity ratio by DEM. Liang et al. [26] developed a parallel-column model for studying heat transfer through granular materials, which accurately predicted the effective thermal conductivity without requiring particle-scale analysis. Nguyen et al. [27] investigated thermal transfer in silo discharge applications, while Sun et al. [28,29] studied the configurational and granular temperature in reciprocating grates. Although numerous studies have investigated CPT and thermal transfer in granular soils using DEM, no previous studies have combined these two subjects to study CPT under heat transfer conditions. This combination represents a major challenge for researchers, but the findings from the above references suggest that DEM simulations can provide insights for solving practical engineering problems in this area.

Our research aims to investigate the influence of temperature on the mechanical behavior of granular soils through 3D DEM simulations of CPT. To achieve this objective, a model of particle expansion was established under heat transfer conditions, incorporating three critical parameters associated with thermal transfer in granular soils: thermal conductivity velocity v_h, specific heat capacity C_v, and particle thermal expansion coefficient α. Then, CPT simulations were conducted on the numerical samples at various temperatures and the particle velocity field and contact forces between particles were examined at the microscopic scale. Our study provides a better understanding of the underlying mechanisms behind the effects of temperature on the mechanical behavior of granular soils, which can inform the design and operation of geotechnical structures in varying thermal environments.

2. DEM Simulation

2.1. Contact Law

The DEM simulations were conducted using PFC 3D 5.0 [30] software, which employs the linear parallel bond contact model to simulate the interaction forces between particles [31–33]. Under this model, if two particles in contact are bonded, the strength linearly increases with elastic deformation until the strength limit is exceeded, and then the bond breaks.

The force-displacement relationship for the linear parallel bond model is calculated by adding the normal force and tangential force, as shown in Equation (1):

$$\overrightarrow{F} = \overrightarrow{F}_n + \overrightarrow{F}_s \quad (1)$$

The parallel-bond surface gap is defined in Equation (2) as the cumulative relative normal displacement of the particle surfaces:

$$g_s = \sum \Delta\delta_n \quad (2)$$

where δ_n is the relative normal-displacement increment of distance between two bonds.

The normal force $\overrightarrow{F}_n$ is calculated by Equation (3):

$$\overrightarrow{F}_n = \overrightarrow{F}_n + k_n A \Delta \overrightarrow{\delta}_n \quad (3)$$

where k_n is the bond normal stiffness, A is the area of the bond cross section, $\Delta \overrightarrow{\delta}_n$ is the relative normal-displacement increment.

The tangential force $\overrightarrow{F}_s$ is calculated by Equation (4):

$$\overrightarrow{F}_s = \overrightarrow{F}_s + k_s A \Delta \overrightarrow{\delta}_s \quad (4)$$

where k_s is the bond tangential stiffness, A is the area of the bond cross section, $\Delta \overrightarrow{\delta}_s$ is the relative tangential-displacement increment.

Figure 1a illustrates the relationship between the normal force $\overrightarrow{F_n}$ and the normal displacement $\overrightarrow{\delta_n}$. It can be observed that the normal force $\overrightarrow{F_n}$ increases with an increase in the normal displacement $\overrightarrow{\delta_n}$. Once the normal force $\overrightarrow{F_n}$ reaches the tensile strength limit, the bond between the two particles breaks, causing the normal force $\overrightarrow{F_n}$ to drop to zero. Similarly, Figure 1b depicts the behavior of the tangential force $\overrightarrow{F_s}$ with respect to the displacement $\overrightarrow{\delta_s}$. The absolute value of the tangential force, denoted as $||F_s||$, is plotted against the absolute value of the summation of $\Delta\delta_s$ on the x-axis, representing the tangential displacement. As the displacement $\overrightarrow{\delta_s}$ increases, the tangential force $\overrightarrow{F_s}$ also increases. It is important to note that once the shear strength limit is reached, if the bond between the two particles breaks, the tangential force $\overrightarrow{F_s}$ decreases to a constant value known as the residual shear strength. Moreover, the bonds will not automatically reestablish even if the two particles come into contact again.

2.2. Thermal Transfer Theory

For thermal transfer DEM simulations, the entire system is treated as a network of heat reservoirs [30], with each particle representing a heat reservoir. At each timestep, a virtual thermal pipe is created between the centroids of two contacted particles, allowing heat to transfer from one heat reservoir to the other [34]. The virtual thermal pipe can be used for heat transfer through the contacting surface.

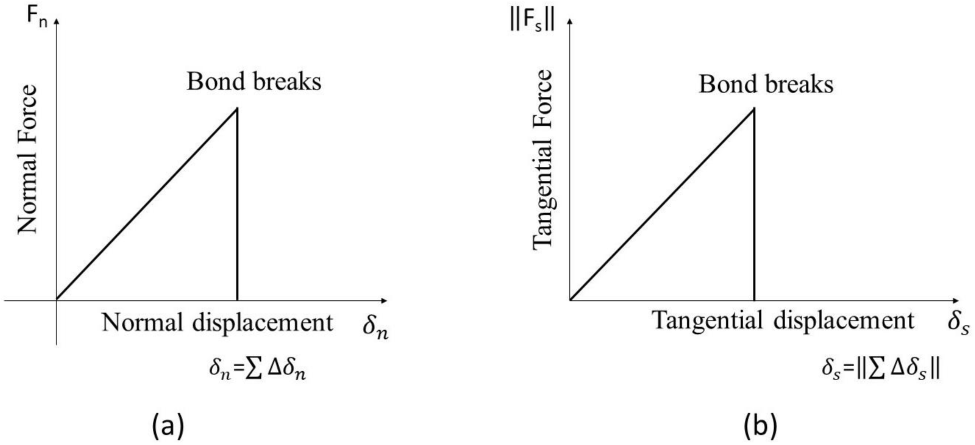

Figure 1. Mechanical responses between two soil disks with parallel bond model: (**a**) Normal force, (**b**) Tangential force.

Fourier's law for a continuum defines the relation between the heat flux vector and the temperature gradient, as shown in Equation (5).

$$q_i = -k_{ij}\frac{\partial T}{\partial x_j} \tag{5}$$

where k_{ij} is the thermal-conductivity tensor w/(m°C).

The average heat flux in a volume, V, of material is defined by Equation (6)

$$< q_i >= \frac{1}{V}\int_V q_i dV \tag{6}$$

where q_i is the heat flux vector acting throughout the volume. By restricting heat to flow only in the thermal pipes, the integral can be replaced by a summation over all M pipes contained within V by Equation (7):

$$< q_i >= \sum_{p=1}^{M} q_i^{(p)} V^{(p)} = \sum_{p=1}^{M} q_i^{(p)} A^{(p)} l^{(p)} \tag{7}$$

where $A^{(p)}$ is the cross-sectional area of the pipe, and $l^{(p)}$ is the length of pipe contained within V.

The thermal resistance per unit length is calculated by Equation (8) as follows:

$$\eta = \frac{1}{3k}\left(\frac{1-n}{\sum_{N_b} V^{(b)}}\right)\sum_{N_p} l^{(p)} \tag{8}$$

where n is the porosity of local particles in measurement, k is the macroscopic conductivity, $V(b)$ is the volume of particle, $l(p)$ is the length of thermal pipe, N_b is the balls with centroids contained within the measurement particle N_p is the active thermal pipes of these particles.

The heat-conduction equation for a single reservoir is calculated by Equation (9):

$$-\sum_{p=1}^{N} Q^(p) + Q_v = mC_v\frac{\partial T}{\partial t} \tag{9}$$

where Q_v is the heat source intensity, m is the thermal mass, and C_v is the specific heat at constant volume.

The following procedure is used to evaluate the thermal conductivity tensor k_{ij} by Equation (10) over a region defined by a measurement sphere.

$$k_{ij} = \frac{1-n}{\sum_{N_b} V^{(b)}} \sum_{Np} \frac{l^{(p)} n_i^{(p)} n_j^{(p)}}{\eta^{(p)}} \tag{10}$$

where V is the volume of ball, n is the porosity within the measurement sphere, n_i and n_j are the unit normal vectors directed along the pipe. η is the thermal resistance.

The power Q is calculated by Equation (11):

$$Q = -\frac{\Delta T}{\eta L} \tag{11}$$

where ΔT is the temperature difference between two reservoirs on each end of the pipe, and L is the pipe length.

The boundary conditions are charged by a constant heat power as the heat resource. The boundary conditions are fixed and undeformable during the thermal transfer stage. The heat from boundary conditions transfers from closer particles to distant particles.

When the temperature increases, the particle expands. The thermal expansion is applied by Equation (12), as follows.

$$\Delta R = \alpha R \Delta T \tag{12}$$

where ΔT is the increment of the temperature, R and ΔR are the initial and variation in particle radius, respectively.

Thermal strains arise due to the thermal expansion of particles. When a mechanical contact is present alongside a thermal contact, thermal expansion of the bond material is taken into account. For linear parallel bonds, it is assumed that only the normal component of the force vector carried by the bond is affected by temperature variations. Assuming an isotropic expansion of the bond material from the bond length, the change in force vector $\Delta \overrightarrow{F}_n$ due to temperature variation can be calculated by Equation (13):

$$\Delta \overrightarrow{F}_n = -k_n A \alpha \overrightarrow{L} \Delta T \tag{13}$$

where k_n is the normal bond stiffness, A is the area of the bond cross-section, α is the expansion coefficient of the bond material, $\overrightarrow{L}$ is the bond length between two heat reservoirs, ΔT is the variation in temperature.

It should be noted that the fluid flow is not considered in the present thermal transfer DEM simulations.

2.3. Simulation Procedure

2.3.1. Sample Generation

A sample consisting of 45,000 soil particles was created within a cubic boundary of dimensions 0.5 m × 0.5 m × 0.5 m. The particle radius varied from 1 cm to 2 cm. The granular sample was subjected to gravity (9.81 m/s^2). The initially generated particles and root particles can overlap, but they adjust their positions under the influence of interaction forces to fill the pores, resulting in a balanced final sample. Then, the upper platen of the cubic boundary was moved up and down 10 times with a velocity of 1 mm/s to compact the sample. Following a series of compactions, the sample's initial porosity was found to be 0.3.

Isotropic consolidation was achieved using a servo-control mechanism, which involved adjusting the positions of all six boundary walls. The pressure exerted on each wall was calculated by dividing the contact force on the wall by its surface area. If the pressure was below the target confining pressure, the wall moved towards the sample to increase the pressure. Conversely, the wall moved away from the sample to release the pressure if the pressure was above the target value. The servo-control mechanism enabled us to gradually adjust the pressure exerted on each wall and eventually reach and maintain the target pressure of 100 kPa. Table 1 presents the DEM parameters of the particles utilized in the simulations [34–36].

Table 1. Parameters of soil particles and wall properties by DEM simulations.

Parameter	Value	Unity
Number of particles, N	45,000	-
Particle radius, r	1∼2	cm
Particle density, ρ	2600	kg/m^3
Local damping coefficient, c	0.7	-
Gap, g_s	0.1	cm
Confining pressure, P	100	kPa
Friction coefficient inter-particles, μ_{gg}	0.3	-
Friction coefficient particle-boundary, μ_{gp}	0.1	-
Normal stiffness of particles, K_{ngg}	8.0×10^7	N/m
Tangent stiffness of particles, K_{sgg}	8.0×10^7	N/m
Tensile strength of bonds, pb_{ten}	500.0	kPa
Cohesion, pb_{coh}	500.0	kPa
Normal stiffness of walls, K_{ngb}	1.5×10^{10}	N/m
Tangent stiffness of walls, K_{sgb}	10^{10}	N/m
Timestep for mechanical study, Δt	1.5×10^{-5}	s/step

2.3.2. Sample Heating Process

In this model, bond formation takes place following compaction but before heating. Compaction is utilized to establish the soil sample's structure, implying that the compacted state represents the desired soil structure for the experiment. Thus, the potential bond breakage resulting from compaction is not taken into account. Meanwhile, bonding bonds play a critical role in promoting heat conduction. Consequently, it is imperative to generate bonding bonds among particles prior to initiating the heating process.

During the heating process, heat was supplied to the sample through the six walls. The heat transferred from the walls to the neighboring particles and then to distant particles. As the temperature of the particles increased, they expanded. The heating process was continued until all particles reached the target temperature.

Table 2 presents the thermal parameters of the particles utilized in the simulations. The specific heat is defined as the amount of heat energy required to raise the temperature of the material by one degree Celsius per unit mass. For this study, the specific heat was assigned a value of 800 J/(kg°C), which corresponds to the specific heat of dry soil [37,38]. The thermal conductivity plays a crucial role in the rate of heat transfer and was set to 1.0 w/(m°C) in the simulations. In order to investigate the impact of different parameters (refer to Section 3.2), the thermal expansion coefficient of the particle was varied.

Table 2. Thermal parameters for preparation of samples at different temperatures.

Thermal Parameter	Value	Unity
Initial temperature of soil, T_s	0	°C
Temperature of heating walls, T_w	10, 20, 30, 40, 50	°C
Specific heat, C_v	800	J/(kg°C)
Thermal conductivity, k	1,3,5,7,9	w/(m°C)
Thermal expansion coefficient of particles, α	$1,2,3,4,5 \times 10^{-3}$	-
Timestep for thermal transfer process, Δt_T	1	s/step

The heating process in this study involves a combination of heat transfer and disk expansion mechanisms, occurring in alternating cycles. However, the extended heating time for the numerical samples renders it impractical to employ a mechanical time step of 1.5×10^{-5} s as the thermal transfer time step. To overcome this limitation, the time step for the thermal transfer mechanism was adjusted to 50 s, accommodating the total heating period of 8000 s. Following each heat transfer mechanism, the disk expansion mechanism is activated. For the disk expansion mechanism, a time step of 1.5×10^{-5} s is employed. However, unlike the thermal transfer process, the disk expansion mechanism does not require a full duration of 50 s before the subsequent heat transfer process. Once the system reaches equilibrium, the disk expansion mechanism pauses and awaits the initiation of the next heat transfer mechanism.

2.4. Simulation of CPT

The CPT model consisted of a cone and a cylindrical shaft. The tip of the cone had an angle of 60° and a diameter of 60 mm. The cylindrical shaft was composed of two sections of rigid cylindrical walls: a frictional cylindrical wall and a frictionless cylindrical wall. The height of the frictional cylindrical wall was 15 mm, while that of the frictionless cylindrical wall was 80 mm. To characterize the dynamic effects in granular systems, the inertial number I was used. The I was calculated using Equation (14).

$$I = \dot{\gamma} d_{mean} \sqrt{\rho / P} \tag{14}$$

where $\dot{\gamma}$ is the shear strain rate, d_{mean} is the mean diameter of the particles, ρ is the density of the particles, and P is the confining pressure. For the quasi-static regime, the value I must be smaller than 10^{-3}. In our research, the CPT penetrated with a velocity of 3 mm/s, which was in the range of CPT penetration velocity proposed by [39].

The tip resistance (q_c) is obtained by summing the contact forces exerted on the tip parallel to the central axis of the penetrometer and dividing it by the penetrometer surface area. Therefore, the cone resistance (q_c) can be calculated using Equation (15):

$$q_c = \frac{F_{cone}}{S_{cone}} \tag{15}$$

where F_{cone} is the total contact force exerted on the tip cone, and S_{cone} is the area of the cone base.

3. Results and Discussions

3.1. Thermal Transfer

The thermal transfer process was investigated in the granular sample during heating to a target temperature of 30 °C. At the start of the heat transfer phase, the temperatures of the six heating walls and sample particles were set to 30 °C and 0 °C, respectively. Figure 2a–d depict the evolution of temperature on the sample surface during the heat transfer process. Initially, heat transferred from the walls to the contacted particles and subsequently from hotter to colder particles. The temperature of the particles close to the twelve edges increased faster than other particles as these were efficiently heated by two approaching walls simultaneously. The temperature evolution inside the sample was also investigated by cross-sections corresponding to Figure 2a–d as shown in Figure 2e–h. The cutting plane passed through the sample center (0, 0, 0) in the direction of the unit vector (0, 1, 0). The cross-sections in Figure 2e reveal that the temperature of particles increased from the exterior towards the interior. The interior of the sample was heated much more slowly than the surface, and when the surface heating was complete, as shown in Figure 2c, the interior was only about 25 °C, as depicted in Figure 2g The heating time of the interior sample, shown in Figure 2h, was longer than that of the surface shown in Figure 2c.

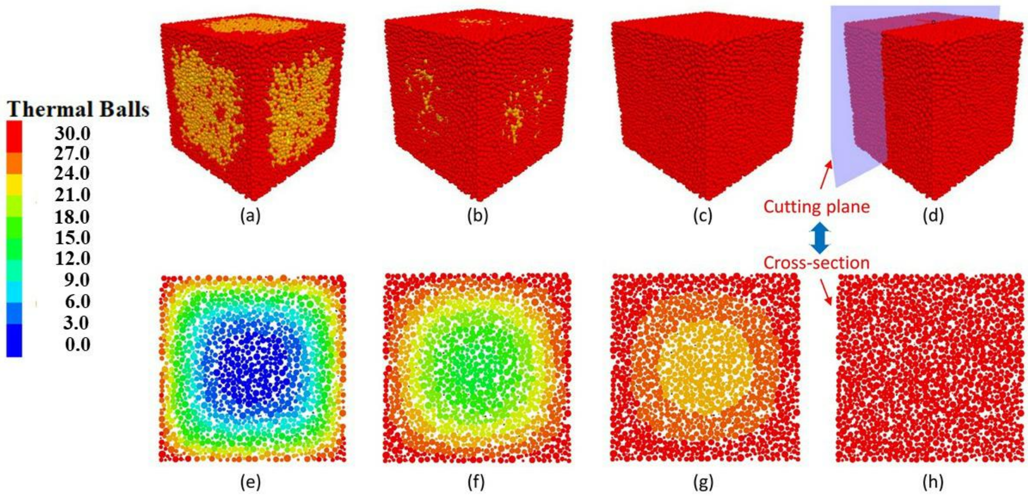

Figure 2. Thermal transfer process on the surface of the sample (**a**–**d**); Corresponding cross-section profiles of interior sample during the thermal transfer process (**e**–**h**).

Influence of Specific Heat

Figure 3 depicts the impact of specific heat C_v on the time required to heat granular soils to various temperatures of 10 °C, 20 °C, 30 °C, 40 °C, and 50 °C. It was observed that an increase in specific heat C_v led to longer heating times for samples to reach the same target temperature. For instance, for a target temperature of 10 °C, samples with C_v = 800 J/(kg°C) and C_v = 1200 J/(kg°C) required 5531 s and 6007 s , for a target temperature of 50 °C, samples with C_v = 800 J/(kg°C) and C_v = 1200 J/(kg°C) required 6479 s and 6707 s, respectively, for complete heating. Similar results were obtained for samples with other specific heat C_v. In the case of constant volume, an increase in specific heat led to an increase in the total heat energy required for the same temperature increment. Consequently, with the same thermal conductivity, the total time needed to heat materials increases.

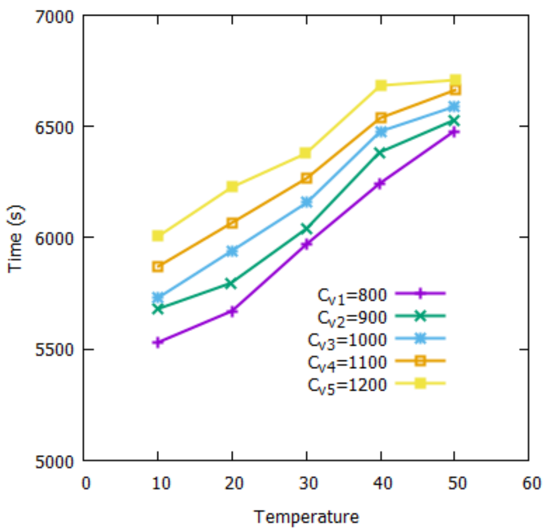

Figure 3. Influence of specific heat on time for heating granular soils to different temperatures 10 °C, 20 °C, 30 °C, 40 °C, 50 °C.

3.2. Influence of the Velocity of Thermal Conductivity

The thermal conductivity of granular media influences the velocity of heat transfer. Figure 4 depicts the effect of thermal conductivity on the time required to heat samples to different temperatures. An increase in the velocity of thermal conductivity leads to a higher heat transfer rate per unit time, reducing the total heating time required. For instance, heating samples to 50 °C using thermal conductivities of v = 1 w/(m°C) and v = 3 w/(m°C) resulted in times of 6013 s and 2040 s, respectively. The significant difference of 3937 s indicates that increasing thermal conductivity from v = 1 w/(m°C) to v = 3 w/(m°C) greatly reduces the total heating time required. However, increasing thermal conductivity from v = 7 w/(m°C) to v = 9 w/(m°C) shortened the heating time to 50 °C from 937 s to 760 s, indicating a small difference of 177 s. These observations demonstrate that increasing thermal conductivity can reduce the time required to heat samples to the same target temperature, but once thermal conductivity is already high, further increases may not significantly reduce the heating time.

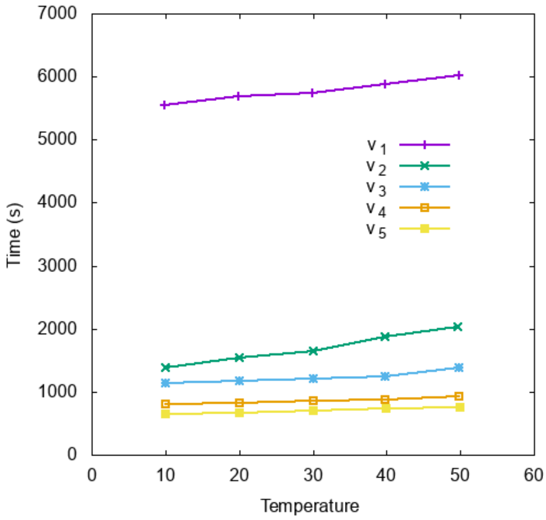

Figure 4. Influence of thermal conductivity on time for heating granular samples to different temperatures 10 °C, 20 °C, 30 °C, 40 °C, 50 °C.

3.3. Influence of Temperatures

The effects of temperature on CPT cone resistance are presented in Figure 5. Five samples were prepared at temperatures ranging from 10 °C to 50 °C, and cone resistance increased as temperature increased. Table 3 shows several results obtained from measuring the mean radius of particles, sample porosities, and cone resistance of the five samples at different temperatures. The mean radius of particles increased from 1.514 cm to 1.576 cm as the temperature increased from 10 °C to 50 °C, while the sample porosity decreased from 0.274 to 0.252. The tip resistance also displayed an increase from 67.2 kPa to 78.1 kPa. These observations indicate that the tip resistances of the CPT increased with increasing temperature due to the expansion of the particles with raised temperature.

Table 3. CPT Results obtained from samples at different temperatures.

Simulation	T	d_{50} (cm)	Porosity n	q_c (kPa)
1	10	1.514	0.274	67.2
2	20	1.529	0.267	69.5
3	30	1.544	0.262	73.3
4	40	1.560	0.258	76.8
5	50	1.576	0.252	78.1

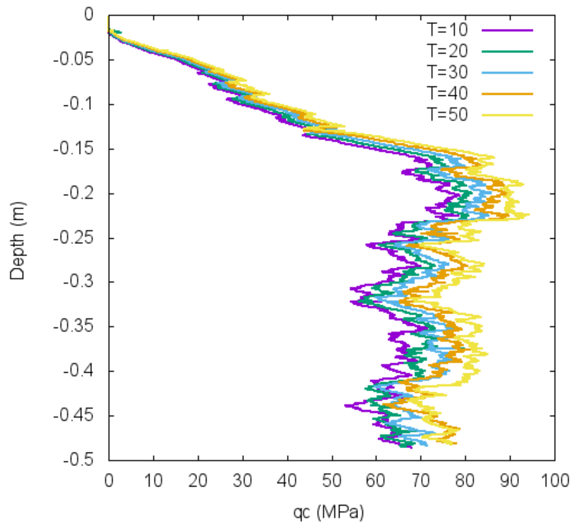

Figure 5. Curves of cone resistances obtained from granular soils at different temperatures.

3.4. Influence of the Thermal Expansion Coefficient

The influence of thermal expansion coefficient α on the cone resistance of CPT is shown in Figure 6. The thermal expansion coefficients of particles were set to different values for comparison: 1×10^{-3}, 2×10^{-3}, 3×10^{-3}, 4×10^{-3}, and 5×10^{-3}. These values were selected to ensure that the particles did not expand excessively per time step, leading to an improper increase in contact force. During the thermal transfer process, particles expand according to their respective thermal expansion coefficients, with greater expansion occurring for particles with higher thermal expansion coefficients. In areas where less free space exists in the granular mass, particles are more constrained when pushed by the cone, resulting in larger zones of highly stressed particles. Figure 6 shows that the cone resistance of CPT increased as the thermal expansion coefficient increased. Table 4 presents the results obtained from CPT simulations conducted with different particle thermal expansion coefficients. As the thermal expansion coefficient increased from 1×10^{-3} to 5×10^{-3}, the mean radius of particles increased from 1.514 cm to 1.592 cm, while the sample porosity decreased from 0.274 to 0.233. Cone resistance also increased from 66.9 kPa to 92.1 kPa.

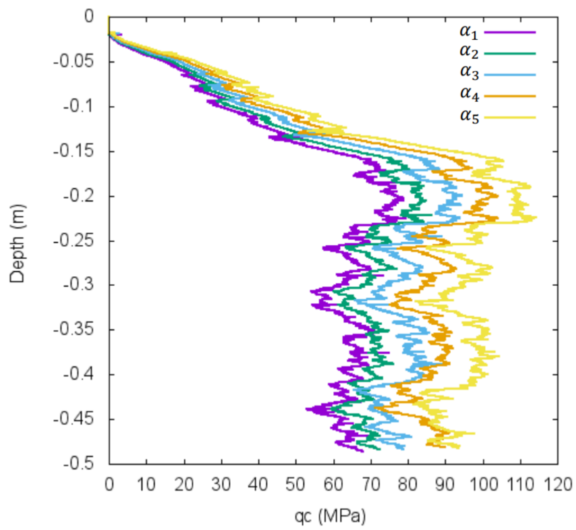

Figure 6. Curves of tip resistance from different coefficients of thermal expansion: 1×10^{-3}, 2×10^{-3}, 3×10^{-3}, 4×10^{-3}, 5×10^{-3}.

Table 4. CPT Results obtained from parametric simulations with particle thermal expansion coefficient.

Simulation	α	d_{50} (cm)	Porosity n	q_c (kPa)
1	1×10^{-3}	1.514	0.274	66.9
2	2×10^{-3}	1.546	0.261	72.1
3	3×10^{-3}	1.574	0.252	79.3
4	4×10^{-3}	1.586	0.243	88.3
5	5×10^{-3}	1.592	0.233	92.1

3.5. Velocity Field of the Soil Particles

Figure 7 present the velocity field of soil particles during the cone penetration process at 10 °C and 50 °C, respectively. The velocity of particles increased as they moved closer to the cone and was observed to be higher in the downward and sideways directions. Near the penetrometer, particles were pushed outwards by the cone, resulting in an uneven distribution of displacement in granular soils. However, displacement was more uniformly distributed far from the cone. Figure 7 illustrates that particles close to the cone were pushed at velocities up to 0.5 m/s during the penetration process. After the cone was fully inserted into the soil, the velocity field of soil particles approximated a circle on the plane holding the cone. These observations are consistent with previous studies. For instance, Huang et al. [40] suggested that the plastic zone around the shaft and behind the cone of a penetrometer is similar to that predicted by cylindrical cavity expansion theory. Falagush et al. [23] demonstrated that the elastic–plastic boundary around the cone tip and face is elliptical or circular. In addition, the velocities of particles at 10 °C were slightly higher than those at 50 °C at t = 0.2 s, as shown by the color zones in Figure 7, which may be due to the higher density of the sample at 50 °C compared to that at 10 °C, limiting the particle movement.

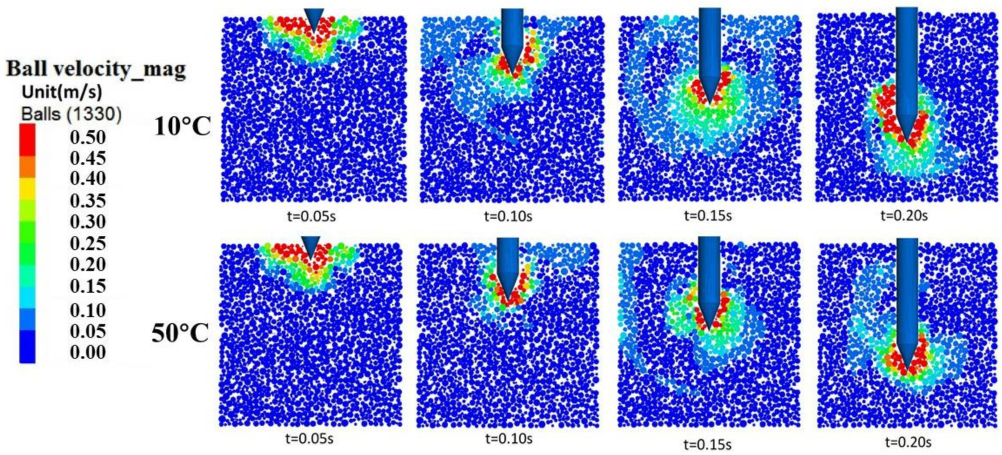

Figure 7. Cross-sections of velocity field in granular soils under 10 °C and 50 °C during the simulation of CPT.

4. Conclusions

In this study, several 3D DEM simulations of CPT in granular soils at different temperatures were conducted. The soil particle system was modeled as a network of heat reservoirs, where each particle represents a single heat reservoir connected by thermal pipes. By performing CPT on several numerical samples, some important conclusions can be drawn, as follows:

- The specific heat C_v and thermal conductivity V_h are significantly affected by the heating time during the thermal transfer process. Generally, the total time required to heat a sample increases as specific heat C_v increases, while it decreases as thermal conductivity V_h increases.

- The sample becomes denser as temperature increases, based on the assumption of particle expansion during the heating process. The cone resistance of the penetrometer also increases with temperature.
- The thermal expansion coefficient of a soil particle is an important factor that affects the density of the sample. The larger the coefficient, the greater the cone resistance of the penetrometer. The velocity field and contact force chain are visualized during CPT, with maximum values occurring near the tip of the cone penetrometer.

Author Contributions: Methodology, investigation, original draft preparation, Y.H.; Software, W.S.; Validation, data curation, H.Y.; conception, writing—review and editing, supervision, K.W. All authors have read and agreed to the published version of the manuscript.

Funding: We gratefully acknowledge the financial supports provided by National Natural Science Foundation of China NO. 51608112, the Fundamental Research'Funds for the Central Universities NO. 2242023K40018.

Data Availability Statement: The data that support the findings of this study are available from the corresponding author upon reasonable request.

Conflicts of Interest: The authors declare no conflict of interest.

Nomenclature

Symbol	**Description**
A	area of the bond cross section
CoR	coefficient of restitution
C_v	specific heat
c	damping coefficient
d_{mean}	mean diameter of the particles
E	particle density
$\overrightarrow{F}_n$	normal force
$\overrightarrow{F}_s$	tangential force
I	inertial number
K_{ngb}	normal stiffness of walls
K_{ngg}	normal stiffness of particles
K_{sgb}	tangent stiffness of walls
K_{sgg}	tangent stiffness of particles
k	macroscopic conductivity
k_n	normal stiffness
k_s	tangential stiffness
$l(p)$	length of thermal pipe
m	mass of particle
n	porosity
$n_{i,j}$	unit normal vector
q_c	cone resistance
T	temperature
$V(b)$	volume of particle
v_h	thermal conductivity velocity
w	angular velocities of particle
α	thermal expansion coefficient of particle
Δt	timestep
$\dot{\gamma}$	shear strain rate
μ_{gb}	friction coefficient particle-boundary
μ_{gg}	friction coefficient inter-particles
ν	poisson's ratio
ρ	density
η	thermal resistance

References

1. Peric, D.; Tran, T.; Miletic, M. Effects of soil anisotropy on a soil structure interaction in a heat exchanger pile. *Comput. Geotech.* **2017**, *86*, 193–202. [CrossRef]
2. Naidu, A.; Singh, D. Field Probe for Measuring Thermal Resistivity of Soils. *J. Geotech. Geoenviron. Eng.* **2004**, *130*, 213–216. [CrossRef]
3. Report, H.R.B.S. (Ed.) *Effects of Temperatures and Heat on Engineering Behavior of Soils*; Highway Research Board: Washington, DC, USA, 1969; Volume 103.
4. Cai, G.; Liu, S.; Puppala, A. Comparison of CPT charts for soil classification using PCPT data: Example from clay deposits in Jiangsu Province, China. *Eng. Geol.* **2011**, *121*, 89–96. [CrossRef]
5. Cai, G.; Liu, S.; Puppala, A. Reliability assessment of CPTU-based pile capacity predictions in soft clay deposits. *Eng. Geol.* **2012**, *141*, 84–91. [CrossRef]
6. Liu, S.; Shao, G.; Du, Y.; Cai, G. Depositional and geotechnical properties of marine clays in Lianyungang, China. *Eng. Geol.* **2011**, *121*, 66–74. [CrossRef]
7. Cai, G.; Liu, S.; Puppala, A. Comparative performance of the international piezocone and China CPT in Jiangsu Quaternary clays of China. *Transp. Geotech.* **2015**, *3*, 1–14. [CrossRef]
8. Motaghedi, H.; Armaghani, D. New method for estimation of soil shear strength parameters using results of piezocone. *Measurement* **2016**, *77*, 132–142. [CrossRef]
9. Kim, R.; Lee, W.; Lee, J.S. Temperature-Compensated Cone Penetration Test Mini-Cone Using Fiber Optic Sensors. *Geotech. Test. J.* **2010**, *33*, 243–252.
10. Staniec, M.; Nowak, H. The application of energy balance at the bare soil surface to predictannual soil temperature distribution. *Energy Build.* **2016**, *127*, 56–65. [CrossRef]
11. Gao, H.; Shao, M. Effects of temperature changes on soil hydraulic properties. *Soil Tillage Res.* **2015**, *153*, 145–154. [CrossRef]
12. Cundall, P.; Strack, O. A discrete numerical model for granular assemblies. *Geotechnique* **1979**, *29*, 47–65. [CrossRef]
13. Jiang, M.; Dai, Y.; Cui, L.; Shen, Z.; Wang, X. Investigating mechanism of inclined CPT in granular ground using DEM. *Granul. Matter* **2014**, *16*, 785–796. [CrossRef]
14. Jiang, M.; Dai, Y.; Shen, Z.; Zhang, N. Distinct Element Analyses of Inclined Cone Penetration Test in Granular Ground. *Powders Grains* **2013**, *1542*, 237–240.
15. Jiang, M.; Yu, H.; Harris, D. Discrete element modelling of deep penetration in granular soils. *Int. J. Numer. Anal. Methods Geomech.* **2006**, *30*, 335–361. [CrossRef]
16. Butlanska, J.; Arroyo, M.; Gens, A. 3D DEM simulations of CPT in sand. *Geotech. Geophys.* **2013**, *1*, 817–824.
17. Butlanska, J.; Arroyo, M.; Gens, A. Size effects on a virtual calibration chamber. In *Numerical Methods in Geotechnical Engineering*; CRC Press: Boca Raton, FL, USA, 2010.
18. Butlanska, J.; Arroyo, M.; Gens, A. Virtual Calibration Chamber CPT on Ticino sand. In Proceedings of the 2nd International Symposium on Cone Penetration Testing, Huntington Beach, CA, USA, 9–11 May 2010; Volume 2.
19. Butlanska, J. Cone Penetration Test in a Virtual Calibration Chamber. Ph.D. Thesis, Universitat Politecnica de Catalunya, Barcelona, Spain, 2014.
20. Ciantia, M.; Arroyo, M.; Butlanska, J.; Gens, A. DEM modelling of cone penetration tests in a double-porosity crushable granular material. *Comput. Geotech.* **2016**, *73*, 109–127. [CrossRef]
21. McDowell, G.; Falagush, O.; Yu, H. A particle refinement method for simulating DEM of cone penetration testing in granular materials. *Geotech. Lett.* **2012**, *2*, 141–147. [CrossRef]
22. Falagush, O.; McDowell, G.; Yu, H. Discrete Element Modeling of Cone Penetration Tests Incorporating Particle Shape and Crushing. *Int. J. Geomech.* **2015**, *15*, 04015003. [CrossRef]
23. Falagush, O.; McDowell, G.; Yu, H.; de Bono, J. Discrete element modelling and cavity expansion analysis of cone penetration testing. *Granul. Matter* **2015**, *17*, 483–495. [CrossRef]
24. Zhong, W.H.; Liu, H.L.; Wang, Q.; Zhang, W.G.; Li, Y.Q.; Ding, X.M.; Chen, L.L. Investigation of the penetration characteristics of snake skin-inspired pile using DEM. *Acta Geotech.* **2021**, *16*, 1849–1865. [CrossRef]
25. Shi, D.D.; Yang, Y.C.; Deng, Y.B.; Xue, J.F. DEM modelling of screw pile penetration in loose granular assemblies considering the effect of drilling velocity ratio. *Granul. Matter* **2019**, *21*, 1–16. [CrossRef]
26. Liang, Y.; Li, X. A new model for heat transfer through the contact network of randomly packed granular material. *Appl. Therm. Eng.* **2014**, *73*, 982–990. [CrossRef]
27. Nguyen, V.; Cogne, C.; Guessasma, M.; Bellenger, E.; Fortin, J. Discrete modeling of granular flow with thermal transfer: Application to the discharge of silos. *Appl. Therm. Eng.* **2009**, *29*, 1846–1853. [CrossRef]
28. Sun, L.; Wang, S.; Lu, H.; Liu, G.; Lu, H.; Liu, Y.; Zhao, F.X. Prediction of configurational and granular temperatures of particles using DEM in reciprocating grates. *Powder Technol.* **2015**, *269*, 495–504. [CrossRef]
29. Sun, L.; Wang, S.; Lu, H.; Liu, G.; Lu, H.; Liu, Y.; Zhao, F. Simulations of configurational and granular temperatures of particles using DEM in roller conveyor. *Powder Technol.* **2014**, *268*, 436–445. [CrossRef]
30. Itasca Consulting Group, Inc. *PFC3D(Particle Flow Code in 3 Dimensions)*; version 5.0; user's manual; Itasca Consulting Group, Inc.: Minneapolis, MN, USA, 2016,
31. Potyondy, D.; Cundall, P. A bonded-particle model for rock. *Int. J. Rock Mech. Min. Sci.* **2004**, *41*, 1329–1364. [CrossRef]

32. Holt, R.; Kjolaas, J.; Larsen, I.; Li, L.; Pillitteri, A.; Sonstebob, E. Comparison between controlled laboratory experiments and discrete particle simulations of the mechanical behaviour of rock. *Int. J. Rock Mech. Min. Sci.* **2005**, *42*, 985–995. [CrossRef]
33. Jiang, M.; Sun, Y.; Li, L.; Zhu, H. Contact behavior of idealized granules bonded in two different interparticle distances: An experimental investigation. *Mech. Mater.* **2012**, *55*, 1–15. [CrossRef]
34. Tomac, I.; Gutierrez, M. Formulation and implementation of coupled forced heat convection and heat conduction in DEM. *Acta Geotech.* **2015**, *10*, 421–433. [CrossRef]
35. Gong, H.; Chen, Y.; Wu, S.L.; Tang, Z.Y.; Liu, C.; Wang, Z.Q.; Fu, D.B.; Zhou, Y.H.; Qi, L. Simulation of canola seedling emergence dynamics under different soil compaction levels using the discrete element method (DEM). *Soil Tillage Res.* **2022**, *223*, 105461. [CrossRef]
36. Liu, L.; Li, W.L.; Lu, Y.L.; Ren, T.S.; Horton, R. Relationship between thermal and electrical conductivity curves of soils with a unimodal pore size distribution: Part 1, A unified series-parallel resistor model. *Geoderma* **2023**, *432*, 116420. [CrossRef]
37. Platts, A.B.; Cameron, D.A.; Ward, J. Improving the performance of Ground Coupled HeatExchangers in unsaturated soils. *Energy Build.* **2015**, *104*, 323–335. [CrossRef]
38. Guo, P.; Wang, Y.; Li, J.; Wang, Y. Thermodynamic analysis of a solar chimney power plant system with soil heat storage. *Appl. Therm. Eng.* **2016**, *100*, 1076–1084. [CrossRef]
39. Janda, A.; Ooi, J. DEM modeling of cone penetration and unconfined compression in cohesive solids. *Powder Technol.* **2016**, *293*, 60–68. [CrossRef]
40. Huang, W.; Sheng, D.; Sloan, S.; Yu, H. Finite element analysis of cone penetration in cohesionless soil. *Comput. Geotech.* **2004**, *31*, 517–528. [CrossRef]

Disclaimer/Publisher's Note: The statements, opinions and data contained in all publications are solely those of the individual author(s) and contributor(s) and not of MDPI and/or the editor(s). MDPI and/or the editor(s) disclaim responsibility for any injury to people or property resulting from any ideas, methods, instructions or products referred to in the content.